Spatial contributions of electron trajectories to high-order-harmonic radiation originating from a semi-infinite gas cell

Martin Kretschmar,[1,2] Carlos Hernández-García,[3] Daniel S. Steingrube,[1,2] Luis Plaja,[3]
Uwe Morgner,[1,2] and Milutin Kovačev[1,2]

[1]*Leibniz Universität Hannover, Institut für Quantenoptik, Welfengarten 1, D-30167 Hannover, Germany*
[2]*QUEST, Centre for Quantum Engineering and Space-Time Research, Welfengarten 1, D-30167 Hannover, Germany*
[3]*Grupo de Investigación en Óptica Extrema, Universidad de Salamanca, E-37008 Salamanca, Spain*

(Received 6 March 2013; published 8 July 2013)

We report on the analysis of the spatial beam profile of high-order harmonic radiation originating from a semi-infinite gas cell (SIGC). We experimentally assign contributions of electron trajectories to different spatial regions of the harmonic radiation beam. The angular divergence of the harmonic radiation is studied for the first time in a SIGC as a function of different phase-matching parameters. We relate the ratio of the dipole phase coefficients to the coherence time and divergence angle measurements. Simulations, including high-order-harmonic propagation, give further insight into the generation process and the influence of phase matching. The analysis reveals that the SIGC enables tuning of the cutoff frequency by altering the absorption of the generating medium.

DOI: 10.1103/PhysRevA.88.013805 PACS number(s): 42.65.Ky, 42.50.Nn

I. INTRODUCTION

High-order-harmonic generation (HHG) has become a common source of coherent light in the extreme ultraviolet (XUV) spectral region and serves as a foundation for a large variety of applications in the field of attosecond science [1–4]. The underlying interaction process between a strong laser field and an atom is well studied and described by the semiclassical three-step model [5] and the quantum mechanical model by Lewenstein *et al.* [6]. Both models exhibit contributions of two electron trajectories to HHG in the spectral plateau region. Their characteristic difference is the excursion time in the continuum, and they are named the long and short trajectories for long and short excursion times, respectively. Experimental studies of the harmonic spatial beam profile in a gas jet setup confirmed theoretical predictions of spatially separated quantum paths [7,8]. It turns out that the difference in excursion time leads to different phase contributions for long and short electron trajectories, which results in distinguishable spatiotemporal characteristics of high-order-harmonic radiation [7–11].

One major requirement, which has to be fulfilled to produce isolated attosecond pulses, is the selection of high-order-harmonic radiation originating from short electron trajectories. Harmonic emission from different electron trajectories accumulates a characteristic attochirp, resulting from the dependence of the recombination time upon the harmonic order. This chirp is positive for the case of short electron trajectories and can be compensated by thin aluminum filters or other similar materials [12–14]. XUV radiation generated by long-electron-trajectory contributions has an opposite negative attochirp, making a compression of these pulses impossible for standard materials. Recent simulations revealed that an off-axis detection of high-order-harmonic radiation originating from trajectory interferences enables the generation of isolated attosecond pulses without the need for chirp compensation [15].

In order to separate the different contributions, their relative weights can be controlled by altering phase-matching parameters during HHG [16]. It has been demonstrated that the ratio of contributions from long and short trajectories can be altered by changing the position of the focus relative to the generating gas jet setup [9]. The separation of the quantum paths can be accomplished with various macroscopic approaches by changing the optical geometry [17–21] or by applying a spatial filter to the harmonic beam [14]. Microscopic selection has also been realized, using a bichromatic electric field to manipulate electron-trajectory contributions [22–25] or by controlling the fundamental electric field [26,27].

The HHG contributions from different quantum paths j exhibit an intensity-dependent atomic phase

$$\phi_j(r,t) \simeq -U_p \tau_{tr}^j \simeq -\alpha_j I(r,t) \tag{1}$$

with a slope α_j correlated to the electrons' traveling time τ_{tr}. This slope is smaller for the short trajectory α_{short} and larger for the long trajectory α_{long} [11]. Consequently, the influence of the atomic phase leads to different phase-matching conditions for contributions from long and short electron trajectories [8]. Bellini *et al.* observed the temporal coherence as well as the spatial beam profile of high-order-harmonic generation originating from a gas jet setup. The experiments prove that long and short electron trajectories lead to the emission of harmonic radiation with different coherence times and divergence angles, corresponding to the slope α of the atomic phase [7,8,28,29]. The spatial profile consists of a central, less divergent part with a longer coherence time compared to an outer, more divergent region with a shorter coherence time. The inner region is associated to short trajectory contributions and the outer region to those from long trajectories [7,8]. Recent experimental studies drew a connection of ringlike structures in the spatial beam profile to long and short electron trajectory interferences [30–32].

The trajectory-specific atomic phase not only influences the spatial properties of high-order harmonic radiation but also their spectral characteristics. Several experiments observed the phenomena of spectral splitting and drew conclusions on the

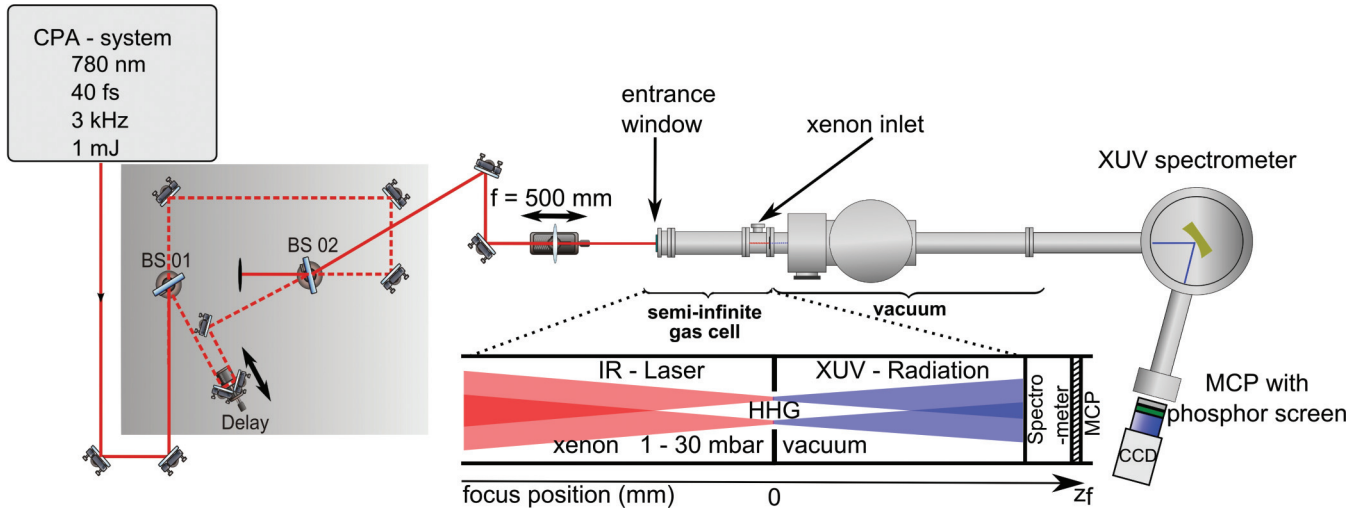

FIG. 1. (Color online) Outline of the experimental setup. The fundamental beam passes a Mach-Zehnder interferometric (MZI) setup before being focused into a semi-infinite gas cell, where high-order-harmonic radiation is generated. The XUV emission is being analyzed by a XUV monochromator, which enables the observation of the spatial beam profile of a single harmonic order. The MZI is used for the identification of electron trajectory contributions, where one arm is slightly misaligned in order to have two phase-locked sources of harmonic radiation.

phase matching of electron trajectories for the gas jet setup [33,34] as well as the semi-infinite gas cell [35].

In this paper, we revisit temporal coherence studies and analyze in detail spatial profiles of harmonic radiation originating from a SIGC. In addition, phase matching of harmonic emission from different electron-trajectory contributions is investigated. The SIGC supports the application of lasers with high repetition rates for HHG, resulting in a higher photon flux for the generated XUV radiation [36–38]. The setup also enables precise control of the pressure of the generating medium. The phase matching of high-order-harmonic radiation originating from a SIGC has already been studied and the results show that focusing further into the gas cell favors generation of higher harmonic orders, whereas focusing at the exit of the cell supports lower harmonic orders. The studies reveal a sharp drop in the overall harmonic yield when placing the focus at the position of the truncating pinhole [39]. The present paper concentrates on the identification of electron-trajectory contributions in the spatial beam profile of high-order harmonic radiation and their dependence on phase-matching parameters in the setup of a SIGC. The studies aim at a controlled selection of XUV radiation with specific attochirp characteristics in order to enable attosecond pulse generation with the aforementioned features of a semi-infinite gas cell.

The paper is organized in three sections. First, we describe the experimental setup and present experimental results, namely spatial profiles of high-order harmonic radiation originating from a semi-infinite gas cell. Next, we perform simulations including high-order-harmonic propagation and therefore phase-matching effects. The last part consists of a discussion of the experimental and simulated results.

II. EXPERIMENTAL SETUP

The experimental setup is presented in Fig. 1. A chirped-pulse amplification system (Dragon, KM Labs Inc.) supplies pulses with a duration of 40 fs with a pulse energy of 1 mJ, centered at a wavelength of 780 nm, at a repetition rate of 3 kHz. In order to identify the electron trajectories, the pulses pass an Mach-Zehnder-type interferometric setup (MZI) before being focused into the SIGC by a 500-mm focal lens. The beam diameter is estimated to be $\approx$40 μm. The chirp of the fundamental pulse has been adjusted in order to compensate for the dispersion accumulated by propagation through air and the focusing lens. The interferometer is used to produce two pulses, which are delayed in time with respect to each other. A piezo electric translation stage is used to precisely control the temporal shift τ between the two pulse replicas. Additionally, the MZI enables a spatial separation of the two pulses, leading to two phase-locked harmonic sources with an estimated distance of 200 μm in the SIGC. The harmonic radiation interferes in the far field, leading to interference fringes in the spatial profile, which allow for coherence time studies [7].

The SIGC consist of an approximately 50-cm-long gas-filled chamber with an adjustable pressure in the range from 1 to 100 mbar. The IR pulses enter the cell through a 2-mm CaF_2 entrance window and are focused close to a metal plate, which represents the end of the SIGC. The high intensity in the focus results in the beam drilling a pinhole into the metal plate, enabling the harmonic radiation to pass into the high vacuum setup for analysis and detection. The size of the pinholes is determined to be in the range of 100–150 μm. The positions z_f given in this paper describe a focus inside the SIGC for negative values and a focus placed inside the vacuum chamber for positive values. The peak intensity for each harmonic source is estimated to be approximately $3.75 \times 10^{14}\,\mathrm{W/cm^2}$ and is approximately a factor of 5 higher than the saturation intensity in xenon. Significant peak shifting due to free electrons occurs only at intensities one order of magnitude higher than the saturation in xenon atoms. Therefore, we can confidentially assume that our measurements are not essentially disturbed by ionization.

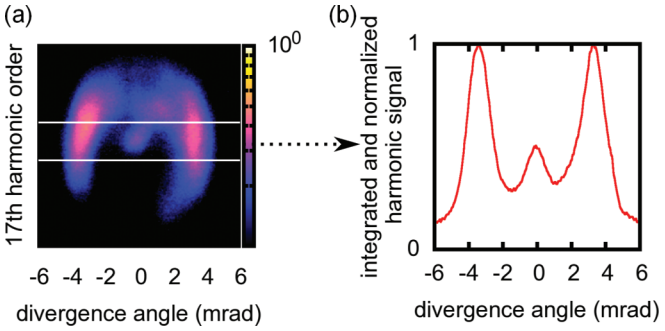

FIG. 2. (Color online) (a) Spatial profile of the 17th harmonic order, generated in 15 mbar xenon at a focusing position of $z_f = -15$ mm. The white box indicates the area which has been cut out for further analysis. The vertical axis correlates with the wavelength axis and the horizontal axis with the spatial axis. (b) Integrated intensity of the spatial profile from the indicated area. The spatial profile clearly consists of two spatially separated contributions, one being on axis around 0 mrad and the other one being off axis at ≈3.8 mrad.

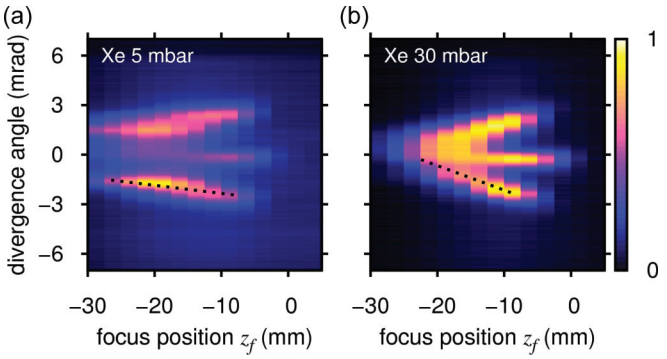

FIG. 3. (Color online) Extracted spatial profiles of the 17th harmonic order versus the focus position z_f in xenon (a) at a pressure of 5 mbar and (b) at a pressure of 30 mbar. The off-axis spatial contributions merge towards the center with decreasing focusing position z_f. The dotted lines sketch slopes of long electron trajectory contributions, which are used for further analysis.

The generated high-order-harmonic radiation propagates an estimated distance of 1670 ± 5 mm until it enters a homemade Seya-Namioka-type monochromator consisting of a 50- × 60-mm toroidal grating with a linewidth of 600 mm^{-1} and a focal length of 625 ± 25 mm. This allows for the analysis of the complete spatial profile of the generated harmonic radiation. Note that we did not use an entrance or exit slit in order to analyze the full spatial profile of the single-order-harmonic radiation. The XUV radiation is detected with a multichannel plate and a phosphor screen setup. The images are recorded with a charged-coupled device (CCD) camera (Hamamatsu Orca II), which is located 1525 mm behind the grating.

III. EXPERIMENTAL RESULTS

We present measurements of the spatial beam profile of single-order-harmonic radiation generated in a SIGC filled with xenon. The data processing is performed in three steps. First, the spatial profile of a single harmonic order is detected. Figure 2(a) shows the spatial beam profile of the 17th harmonic order originating from 15 mbar xenon. The harmonic orders are separated along the vertical axis of the recorded profile, while the horizontal axis gives information about spatial contributions and the divergence of the recorded harmonic order. The signal exhibits a central, less divergent part which is surrounded by a ring structure emitted at high divergence symmetrically around the axis. The divergence angle θ is determined by assuming that the harmonic radiation is generated in a point source close to the optical axis at the position of the pinhole.

Second, to further analyze the profiles, an integrated lineout [indicated in Fig. 2(a)] is taken from the spatial beam profile. We choose to place the cuts along the spatial axis in order to avoid spectral effects on the analyzed spatial profiles. The resulting intensity profile is presented in Fig. 2(b), retaining the spatial features of the high-order-harmonic radiation.

Third, the recorded harmonic profiles are further investigated in dependence of the focus position and gas pressure inside the SIGC. Figures 3(a) and 3(b) show vertical slices of the beam profiles in the case of the 17th harmonic order versus the focus position at two different xenon pressures of 5 and 30 mbar. For a pressure of 30 mbar of xenon, the on-axis and the off-axis contributions appear to overlap and merge at a focus position $z_f \lesssim -20$ mm inside the SIGC relative to the pinhole. By translating the focus in the direction of the exit pinhole, the ring structure exhibits an increasing divergence angle θ, which well separates the on-axis from the off-axis contributions.

We further examine the response of the spatial profile of the harmonic radiation in dependence of the gas pressure inside the SIGC for a fixed focusing position. Figure 4(a) depicts converging spatial contributions with increasing pressure at a focusing position of $z_f = -15$ mm and xenon pressures between 2 and 30 mbar.

To further investigate the dependence of the divergence angle of the off-axis structure upon the pressure, a linear fit is applied to the center of gravity of the off-axis contributions in dependence of the focus position (compare black-dotted lines in Fig. 3). Figure 4(b) shows the evaluated slopes versus the

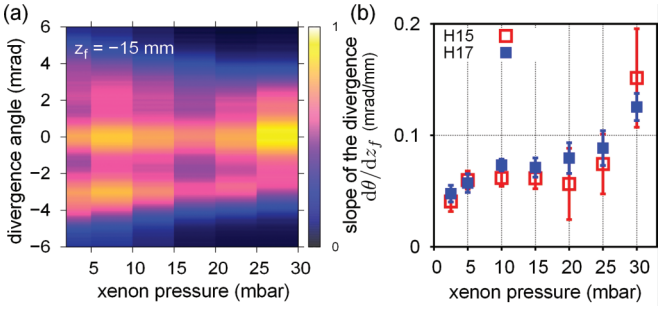

FIG. 4. (Color online) (a) Spatial profile of the 17th HO versus the pressure inside the SIGC. The focus position is fixed at $z_f = -15$ mm. A merging behavior of the spatial contributions is again observed. The color encodes the normalized linear intensity. (b) Slopes of the divergence of the outer ring structure versus focus position at different pressures. The slopes of the 15th (hollow square, red online) and 17th (solid square, blue online) harmonic order are illustrated. The error bars indicate the least square difference of the linear fit.

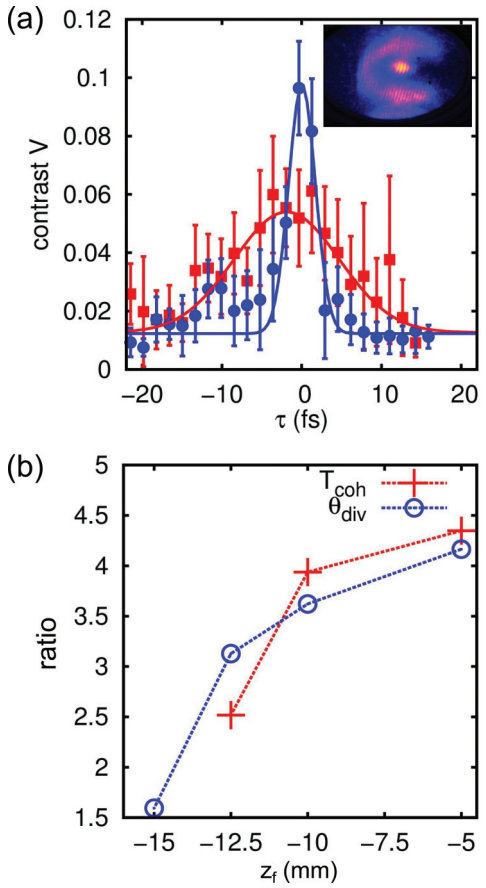

FIG. 5. (Color online) (a) Determination of the intensity contrast of spatial interference fringes for the 17th harmonic in dependence of the delay τ_d between two HHG sources at $z_f = -10$ mm and a pressure of 20 mbar. The inset displays the spatial profile with interference fringes. The contrast V is determined for the on-axis (square, red online) and off-axis (dot, blue online) region, respectively (cf. Fig. 3). The error bars indicate the standard deviation of the contrast evaluated over multiple measurements. The solid lines illustrate a fit to a Gaussian function to determine the coherence time via the FWHM. (b) Comparison between the ratio of the determined coherence time of on- and off-axis contributions $[T_{coh}(\text{on})/T_{coh}(\text{off})]$ and the ratio between their divergence angles $[\Theta_{div}(\text{off})/\Theta_{div}(\text{on})]$ for spatial beam profiles of the 17th harmonic order originating from 20 mbar xenon at different z_f.

pressure for the 15th and 17th harmonic orders. Increasing the gas pressure inside the SIGC leads to a steeper slope of the off-axis contribution, meaning the on- and off-axis contributions merge more drastically towards each other at higher pressures and overlap at a position closer to the pinhole.

In order to identify the contributions from different trajectories in the SIGC setup, we perform measurements of the coherence time $T_{coh} \propto 1/\alpha$ in the on-axis and off-axis spatial regions, respectively. The recorded interference fringes in the beam profile are analyzed by their intensity contrast $V = (I_{max} - I_{min})/(I_{max} + I_{min})$. The contrast is evaluated for different delays τ_d between the two arms of the interferometer. Therefrom, the coherence time T_{coh} can be calculated by the FWHM of the contrast function $V(\tau_d)$ [7]. Figure 5(a) illustrates the contrast V of the 17th harmonic in dependence of the temporal delay τ_d measured in the on-axis and off-axis regions, respectively. The dots (blue online) indicate the visibility of the off-axis contribution and the boxes (red online) indicate the visibility of the on-axis contribution. Each point represents an average value of 10 single shots with its standard deviation given by the error bars. From a Gaussian fit to the contrast $V(\tau_d)$, we determine the coherence time T_{coh} to 15.5 ± 2.9 fs in the on-axis region and 3.9 ± 0.6 fs in the off-axis region.

According to the relation $T_{coh} \propto 1/\alpha$, the on-axis harmonic radiation is attributed to a smaller slope factor α_{short}, indicating the contribution of short electron trajectories to harmonic radiation. Due to its shorter coherence time, the off-axis part is assigned to the long trajectory α_{long}. This agrees well with existing measurements of the coherence time made in a gas jet geometry [7,8,31]. For the experimental conditions in Fig. 5(a), we determine a ratio between the coherence times $T_{coh}(\text{short})/T_{coh}(\text{long}) \propto \alpha_{long}/\alpha_{short}$ of $\nu_{coh} = 3.9 \pm 0.6$.

From the measured harmonic profile of the 17th harmonic order in 20 mbar xenon, we estimate the divergence angle via the FWHM of a Gaussian fit to the different areas $\theta_{short} \approx 1.08$ mrad and $\theta_{long} \approx 3.91$ mrad of the on-axis and off-axis radiation, respectively. The larger divergence of the long trajectory contribution is in accordance with the relation $\theta \propto \alpha$, derived in a geometrical optics approximation [40]. This allows us to compare the quotient $\nu_{coh} = 3.9 \pm 0.6$ determined via the coherence time to the quotient $\nu_\theta = \theta_{long}/\theta_{short} \propto \alpha_{long}/\alpha_{short} \approx 3.62$ determined via the divergence angles, which are in very good agreement. In order to distinguish if the macroscopic measurement of the beam profile reveals microscopic features of the phase slope α, obtained by the coherence time, the given ratios have been evaluated for different focusing positions z_f at a xenon pressure of 20 mbar. This is illustrated in Fig. 5(b). We observe that the ratio ν_{coh} obtained by the coherence times correlates with the ratio ν_θ obtained by the divergence angles. This indicates that the difference in coherence between the on- and off-axis contributions can be observed by their divergence angles θ, meaning that we can directly see contributions of long and short electron trajectories and their microscopic relation by simply observing the spatial beam profile.

In order to exclude the observation of ringlike structures originating from interference effects between long and short trajectory contributions, we compare the experimental results to simulated high-order-harmonic profiles which include these interferences [30,41]. The simulations also help us to understand the underlying generation process and explain the merging behavior of the electron trajectory contributions.

IV. SIMULATIONS

For further investigations, we carry out theoretical simulations including high-order-harmonic propagation. Our propagation code [41] is based on the integral solution of the wave equation $E(r,t) = E_0(r,t) + E_i(r,t)$, where $E_0(r,t)$ is the fundamental field as it propagates in vacuum, and $E_i(r,t)$ is the field radiated by the elementary sources in the target,

$$E_i(r,t) = -\frac{1}{c^2}\int dr' \frac{1}{|r-r'|}\left[\frac{\partial}{\partial t'}J(r',t')\right]_{t'=t-|r-r'|/c}, \quad (2)$$

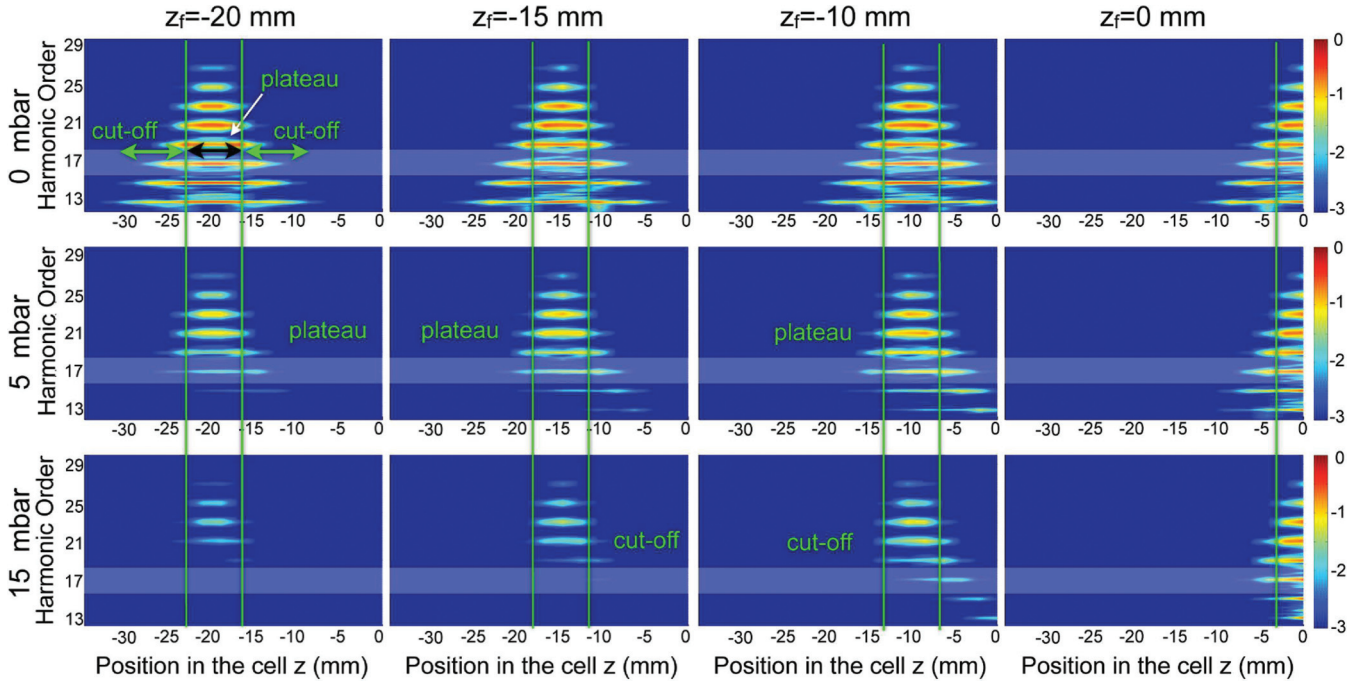

FIG. 6. (Color online) Single-atom HHG spectrum along the propagation axis weighted by the absorption over the length remaining until the end of the SIGC ($z_f = 0$ mm). The focus position is changed from the left ($z_f = -20$ mm) to the right ($z_f = 0$ mm). From top to the bottom the absorption increases with rising gas pressure: From no absorption (0 mbar) in the first row to an absorption corresponding to 15 mbar in the third one. Radiation below the 19th harmonic order is strongly influenced by the absorption properties of xenon. The indicated gray (green online) lines display the area in which the observed 17th harmonic order belongs to the plateau or the cutoff region of the high-order-harmonic spectrum.

where J is the current density. Note that this expression assumes, that the generated radiation propagates with the vacuum velocity c, which is reasonable for the high harmonics. The total harmonic field at the detector is the coherent addition of the elementary contributions from each point of the target. We apply the discrete dipole approximation over the target in order to speed up the calculations [41]. Propagation effects in the fundamental field such as the free charges and neutrals, as well as absorption in the propagation of the harmonics, are also taken into account.

In order to compute the radiated field of each elementary source in the target, we use the single-atom harmonic radiator solver, which computes the harmonic radiation from a single atom for the particular form of the electromagnetic field at the position of the atom. This radiator solver is based on the strong-field approximation + (SFA+) theory [42], an extension of the conventional strong-field approximation approach [6,43]. The SFA+ method allows computation of the harmonic spectrum including the complete momentum space and includes the field dressing of the ground state to give an accurate quantitative description of the harmonic spectrum. Our calculations are performed in xenon, using the Roothaan-Hartree-Fock wave function [44] for the ionization and rescattering matrix elements. The acceleration operator for hydrogen in Ref. [42] is replaced accordingly with the gradient of the Coulomb potential of the xenon ion [45]. This method has formerly been used to observe the effects of trajectory interferences on the generation of attosecond pulses in a gas jet setup [15], as well as to study the interplay between the longitudinal and transversal coherence length [46]. Here we expand it to the SIGC setup to match our experimental conditions. We perform our computations assuming a 5.8-cycle (15-fs) FWHM $\sin^2$ pulse, centered at 780 nm, with an intensity at the focus of $\simeq 1.3 \times 10^{14}$ W/cm^2. The beam is assumed to be polarized along the x direction and to be of a spatial Gaussian profile (propagating along the z direction). The beam is taken directly as input to the calculations. The beam waist at the focus is 38 μm. The SIGC is modeled by an homogeneous xenon slab (i.e., cell), 4 cm in length and of variable density (10^{17} to 10^{18} atoms/cm^3).

Before implementing the complete propagation and phase-matching effects, we concentrate solely on the effect of absorption upon the single-atom high-harmonic generation. In Fig. 6 we present the single-atom HHG spectra along the propagation direction calculated at focusing positions z_f of 0 mm, -10 mm, -15 mm, and -20 mm (left to right) along a xenon-filled SIGC at different pressures of 0 mbar, 5 mbar, and 15 mbar (top to bottom), assuming the ideal gases law at a temperature of 295 K. The 17th harmonic order, which is the experimentally observed order, is highlighted in each plot. In the first row in Fig. 6, corresponding to 0 mbar and consequently no absorption, it can be seen that the 17th harmonic order can be either generated in the plateau region of the harmonic spectrum or in the cutoff. The harmonic is generated in the plateau if its origin is in the center of the focus. The intensity distribution along the focus also allows for the generation of the 17th harmonic order in the wings of the focus, in which the observed harmonic order falls into

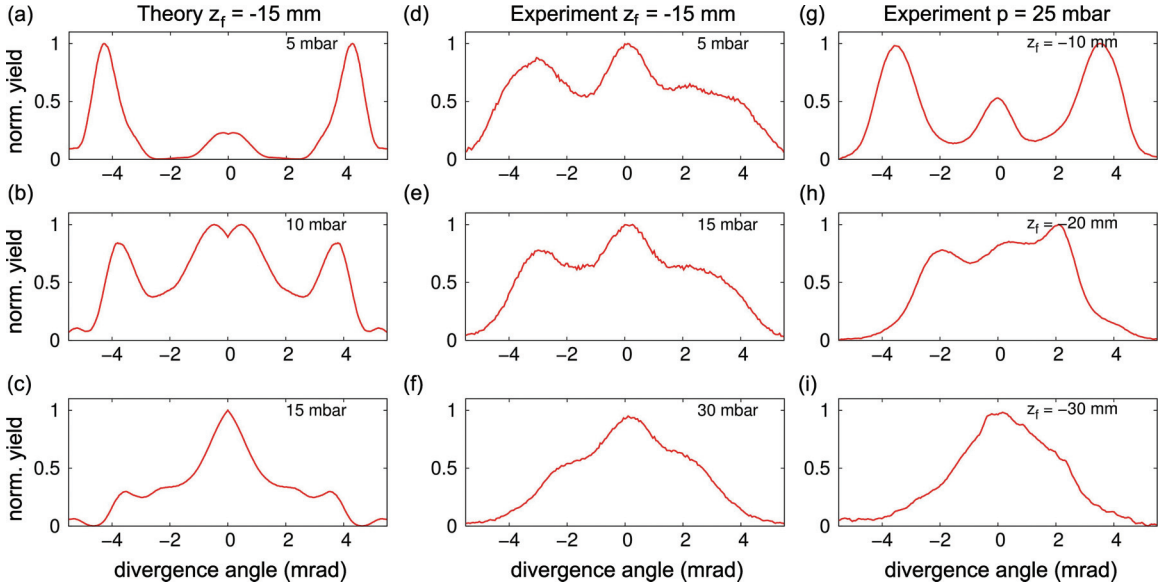

FIG. 7. (Color online) Comparison between the simulated and experimental spatial profiles of the 17th harmonic order. In the left column the simulated profile is shown for a focus placed at $z_f = -15$ mm, at xenon pressures of (a) 5 mbar, (b) 10 mbar, and (c) 15 mbar. In the middle column, we present the experimentally obtained spatial profiles. The profiles are extracted at $z_f = -15$ mm, according to the simulated profiles. The pressure inside the SIGC corresponds to (d) 5 mbar, (e) 15 mbar, and (f) 30 mbar. The plots are chosen to match the simulated results, revealing that simulated profiles according to a parameter set of $z_f = -15$ mm and 15 mbar correspond to experimental results of $z_f = -15$ mm and 30 mbar. The right-hand column displays experimentally obtained spatial profiles recorded at different focusing positions at a fixed pressure of 25 mbar. The focus is placed at (g) -10 mm, (h) -20 mm, and (i) -30 mm.

the cutoff area of the harmonic spectrum due to the decrease of the peak intensity. This can be observed in detail in Fig. 6 in the plot in first column, corresponding to a focusing position of $z_f = -20$ mm, and the first row, corresponding to 0 mbar and no absorption. In between positions of -18 mm and -23 mm, the 17th harmonic belongs to the plateau, indicated by the gray (green online) lines, whereas outside of this area it belongs to the cutoff. The detected signal at the end of the SIGC corresponds to the integration over the cell's position; therefore the dominating signal at the detector will be the one originating from the central part of the focus, belonging to the plateau region.

In the following, we analyze how absorption plays a significant role in selecting the region, from which harmonic radiation is detected. As can be seen in the plots in the third row of Fig. 6, the absorption suppresses the 17th harmonic radiated before and in the center of the focal area. Let us concentrate on a focusing position of $z_f = -10$ mm. For the case of low absorption at a pressure of 5 mbars, the detected signal of the 17th harmonic order belongs to the plateau. Increasing the gas pressure inside the SIGC increases the absorption, and thus, the effective area where the detected harmonics are generated is shifted to the positive wing of the focus. The stated arguments also apply for a fixed pressure and a changing focusing position, since the final absorption of the harmonic is equally influenced either by the increase of the absorption coefficient or the extension of the propagation distance.

In order to compare the simulated spatial profiles with our experimental data, we extend the simulations from single-atom SFA + with absorption to include propagation and therefore phase-matching effects [41]. Figures 7(a)–7(c) present the simulated spatial high-order-harmonic profiles for a fixed focusing position of $z_f = -15$ mm and xenon pressures of 5, 10, and 15 mbar. The central column, showing plots 7(d)–7(f), contains the angular profile of the harmonic detected in the experiment at a fixed position of $z_f = -15$ mm and pressures of 5, 15, and 30 mbar. As already mentioned, a change of the xenon gas pressure influences the absorption properties in a way similar to a change of the focus position in the gas cell. Therefore, we also present matching experimental profiles at a fixed pressure of 25 mbar and different focusing positions of $z_f = -10$ mm, $z_f = -20$ mm, and $z_f = -30$ mm in Figs. 7(g)–7(i). Note that the respective spatial profiles are normalized to their peak value in order to enable a direct comparison of the spatial beam profiles of the harmonic radiation. The absolute value of the harmonic yield is dependent on the phase-matching conditions in the gas cell and decreases in the simulations [along the profiles in Figs. 7(a) to 7(c)] by a factor of 13. The experimental data do not reveal the absolute harmonic yield. The signal evolution of the relative yield shows a drop-off by a factor of 10 [along the profiles in Figs. 7(g)–7(i)7(i)]. The equal drop-off of the signal in the simulations and the experimental data supports our assumption of comparable generating intensities for the chosen phase-matching conditions. By comparing the theoretical and experimental results, it can be seen that the merging behavior of the on- and off-axis contributions could be well reproduced, but the xenon pressures at which the spatial distributions overlap differ between the simulations and the experiments.

This can be readily explained by the difference in intensity used in the simulation, compared with the experiment.

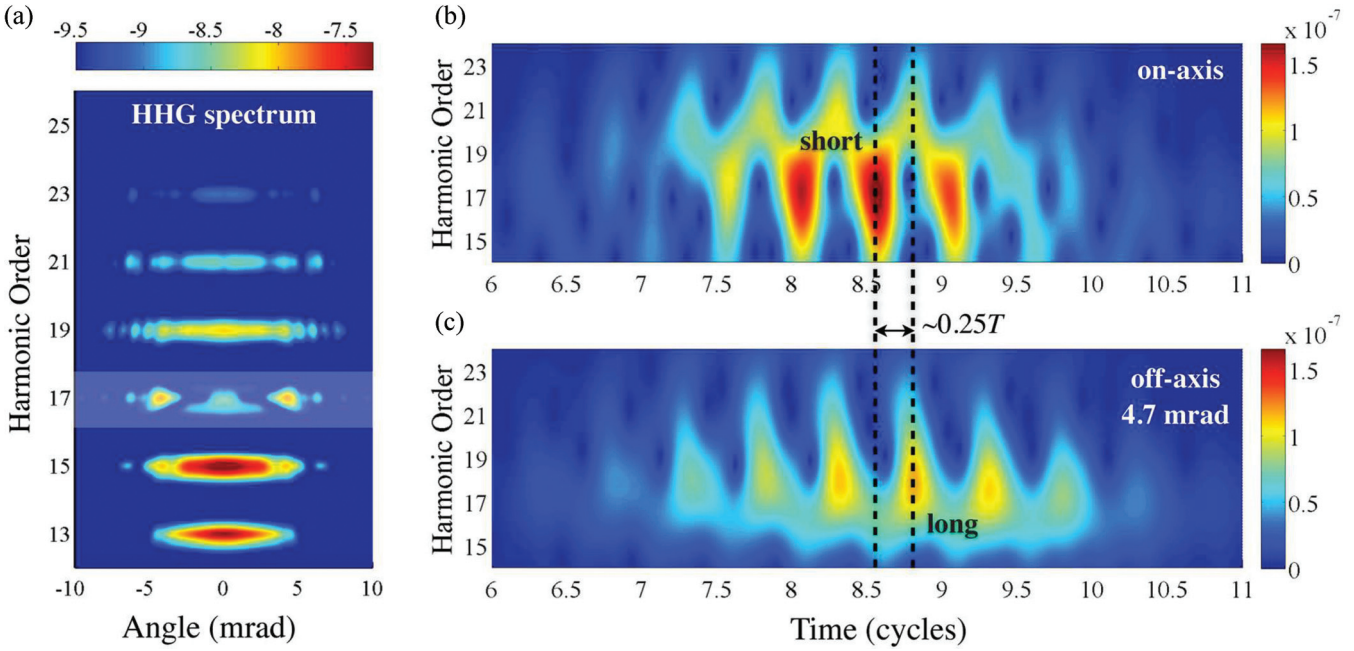

FIG. 8. (Color online) (a) HHG spectrum simulated in a 5-mbar gas cell, when the focus is placed at $z_f = -15$ mm. The time-frequency analysis is presented for the harmonics detected (b) on axis and (c) 4.7 mrad off axis. The color scale denotes the yield of the time-frequency analysis. The HHG spectrum was modified in order to enhance the visibility of the 17th harmonic in the time-frequency analysis. The emission time of the 17th harmonic differs in $0.25T$ from on-axis to off-axis contributions, where T denotes the period of the laser field. This theoretically proves the contribution of long and short electron trajectories to the high-order-harmonic beam profile.

In the experiment, the peak intensity is estimated to be 3.75×10^{14} W/cm^2. This falls above the intensity limitation of the simulations, as those high intensities correspond to the barrier suppression regime, in which the applied SFA + is not reliable. For this reason, the peak intensity in the simulations is chosen to be 1.26×10^{14} W/cm^2. The difference in the peak intensity influences the direct one-to-one comparison of the simulated and experimental results, since a higher peak intensity of the focus also results in a higher intensity in the wings of the focus. Consequently, the experimentally observed 17th harmonic order is generated over a larger region in the gas cell around the focus position. This is being compensated by increasing the absorption coefficient using higher pressures or by moving the focus further into the SIGC. Both situations correspond to Fig. 7(a) (theory) and Fig. 7(g) (experiment), where the spatial profiles can be considered equivalent. The generating intensity is equal, although the peak intensity in the experiment is three times higher than in the simulations. This is due to the different absorption properties in the simulations and the experiment. From this initial situation, increasing the depth of the focal position will cause the harmonics to be generated at a lower intensity region of the Gaussian tail and, therefore, closer to the plateau's cutoff. As discussed before, this intensity reduction is equivalent to leaving the focus position fixed and increasing the gas pressure (i.e., the absorption coefficient). The pairs of figures in Figs. 7(a) and 7(g), Figs. 7(b) and 7(h), and Figs. 7(c) and 7(i) demonstrate that, in both situations, the spatial harmonic profile evolves from a structure obtained from plateau harmonic orders to a structure corresponding to harmonic radiation originating from the cutoff.

A further insight of this process can be gained by performing a time-frequency analysis of the spectrum at different detection angles. To enhance the visibility of the 17th harmonic in the time-frequency analysis, we have reduced artificially the amplitude of the 15th and 19th harmonics, so the 17th harmonic is the prominent one. Now, when performing the time-frequency analysis with a Gaussian window of $2.5 \times \omega_0$, where ω_0 represents the fundamental frequency, the obtained information is mainly valid for the 17th harmonic order. In Fig. 8, we show the simulated HHG spectrum for a focusing position of $z_f = -15$ mm and a xenon gas pressure of 5 mbar, corresponding to Fig. 7(a). The other figures show the time-resolved emission yield of the high harmonics when detected (b) on axis and (c) at 4.7 mrad off axis. We observe that the emission time of the 17th harmonic differs in $0.25T$ from on to off axis. Looking at the evolution of the harmonic signal along the temporal axis, we observe that the signal in Fig. 8(b) is positively chirped, whereas the signal in Fig. 8(c) is negatively chirped. This confirms the short trajectory origin of the central peak and the long trajectory origin of the outer structure.

V. DISCUSSION

In this section, we study further the experimental results from Figs. 3 and 4. We concentrate on the explanation of the decreasing divergence angle of the off-axis contributions in dependence of a decreasing focusing position or an increasing pressure.

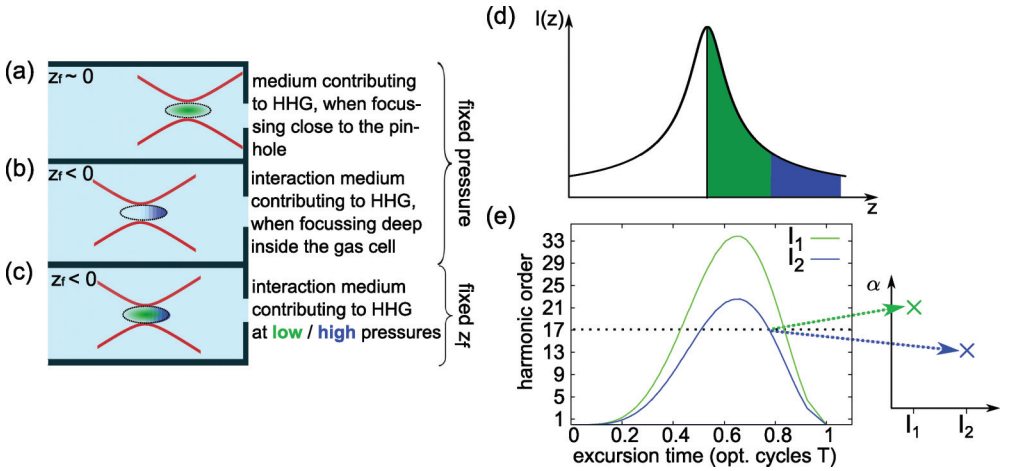

FIG. 9. (Color online) Sketch explaining the dependence of the divergence angle θ of the off-axis contributions upon the pressure and the focusing position (see text for details). The red (gray) solid lines illustrate the beam waist of the fundamental field. Panels (a) and (b) display the effect of moving the focus into the SIGC at a fixed pressure. The regions from which high-order-harmonic radiation is detected are plotted in green (light gray) and blue (dark gray), respectively. Panel (c) shows these contributing regions in blue (dark gray) for a high-pressure p_h and in green (light gray) for a low-pressure p_l at a fixed focusing position well inside the SIGC. The intensity $I(z)$ of the fundamental field, corresponding to the sketched regions in panels (a)–(c), is displayed in panel (d). In panel (e), we present the excursion time of electrons in the continuum vs the generated harmonic order for two intensities corresponding to the green (light gray) and blue (dak gray) regions. The black dotted line illustrates the position of the observed 17th harmonic order. Next to it, we sketch the corresponding phase slope factors α_{long} of the atomic phase for long electron trajectory contributions. They depend on the intensity I at which HHG takes place, since the observed harmonic order shifts closer to the spectral cutoff. Therefore, α_{long} is dependent on z_f and the pressure.

Figure 9 serves as a guideline for our discussion. In Figs. 9(a) and 9(b), we sketch the case of different focusing positions in the SIGC for a fixed pressure. In the experiment, we observe that the divergence angle θ of the off-axis contributions decreases, when moving the focus position from the exit of the SIGC [compare Fig. 9(a)] into the gas cell [Fig. 9(b)]. Within our notation, this corresponds to a decreasing focusing position z_f. This results in an increasing influence of absorption upon the detected high-order-harmonic radiation, which is well confirmed in the simulations in Fig. 6. The harmonic signal is confined to HHG from an effective generation volume V_{eff}, which is strongly dependent on reabsorption in the generating medium and therefore dependent on z_f. In the case of z_f being close to the exit of the SIGC, sketched in gray (green online) in Fig. 9(a), the detected harmonic signal results from an area V_{eff} in the center of the focus. Translating z_f into the SIGC leads to reabsorption of harmonic radiation generated in the center. Therefore, the detected harmonic signal consists of radiation originating from an effective area V_{eff} which is located in the wing of the focus. This region is displayed in blue (dark gray) in Fig. 9(b). The change of z_f affects the resulting spatial beam profile of the observed 17th harmonic order in two different ways.

On the one hand, the electron trajectory contributions are effected by the change of V_{eff} and the resulting change of the generating intensity, which is sketched in Fig. 9(d). A shift of the focus into the gas cell leads to a decreased intensity in V_{eff}. As it is illustrated in Fig. 9(e), this results in a decline of the harmonic cutoff frequency, compared to conditions in the center of the focus. The decreasing spectral distance of the observed and highlighted 17th harmonic order (black-dotted lines) to the cutoff is shown and can as well be traced in the simulations in Fig. 6. For a fixed harmonic order, this means that the excursion times of the two participating electron trajectories and therefore their phase slopes α of the atomic phase merge with decreasing intensity and accordingly with decreasing z_f. The slopes of the long electron-trajectory contributions in dependence of the intensity are presented in Fig. 9(e) as well. The converging behavior of the phase slopes α_{long} (corresponding to long electron trajectories) and α_{short} (corresponding to short electron trajectories) directly translates to the spatial properties of the harmonic radiation, since the divergence angle is directly proportional to the phase slopes $\theta \propto \alpha$. Experimentally (see Fig. 5) as well as theoretically (Fig. 8), we could prove that the off-axis structure in the spatial beam profile corresponds to harmonic radiation from long electron trajectories. This means that the off-axis phase coefficients diminish with decreasing intensity, as sketched in the right plot in Fig. 9(e). By this we can well explain the observed spatial structures in the harmonic beam profile and their merging behavior with decreasing z_f [8,28,47].

On the other hand, moving the effective generation region into the wings of the focus not only has an influence upon the peak intensity, but on the phase-matching conditions for both electron trajectory contributions as well. The interplay between the atomic phase, accumulated during the excursion of the electrons on their respective trajectories, and the Gouy phase influences the phase matching of the electron-trajectory contributions to HHG. In the center of the focus the total phase variation is much more pronounced, leading to a favored off-axis phase matching of long electron-trajectory contributions, whereas in the wings, this phase distortion is much smaller, resulting in good phase-matching condition closer to the axis [48,49]. Consequently, the long electron-trajectory

contributions are emitted closer to the optical axis, in the wings of the focus in comparison to their generation in the center of the focus.

The dependence of the divergence angle upon the pressure inside the gas cell (compare Fig. 4) can be explained by similar arguments. In Fig. 9(c), we sketch the case of a fixed focusing position well inside the SIGC at two different gas pressures. Considering a high pressure p_h, we obtain an effective interaction volume $V_{eff}(p_h)$, which is confined in a small region before the pinhole due to absorption (sketched in blue [gray] in Fig. 9). As above, a low-intensity $I_{z_f}(p_h)$ inside V_{eff} results in a low divergence $\theta(I_{z_f}(p_h)) \equiv \theta(p_h)$ of the long trajectory. In the case of a low-pressure p_l, the interaction volume $V_{eff}(p_l)$ is enlarged due to an increased absorption length. Thus, at the same focus position, the maximum intensity $I_{z_f}(p_l)$ contributing to HHG is enhanced, as sketched in green [gray] in Fig. 9(d). This results in a higher divergence for a lower pressure: $\theta(I_{z_f}(p_l)) \equiv \theta(p_l) > \theta(p_h)$, which is in good agreement with the measurements in Fig. 4(a). In our experimental findings in Fig. 4(b), we conclude that the slope of the divergence angle in dependence of the focusing position $d\theta/dz_f$ increases with rising gas pressure, which can be well explained by the given arguments. Effects of reabsorption influence the harmonic signal more rapidly, when moving the focus into the SIGC at higher pressures compared to low gas pressures. Consequently, the smaller divergence angle $\theta(p_h)$ for a high pressure at a fixed focus position $z_f < 0$ causes a steeper slope $d\theta/dz_f$ of the divergence angle θ versus focus position z_f in agreement with the experiment.

This enables a spatial separation of the long and short trajectories at certain phase-matching parameters. In comparison to the gas jet configuration, where one is able to isolate the short trajectory contributions by phase matching, the SIGC supports selection of the short trajectory contributions by placing an iris in the high-harmonic radiation beam. One distinct feature of the SIGC setup is the possibility to tune the cutoff by altering the focusing position z_f inside the SIGC. With the arguments given above, one can decrease the cutoff by moving the focal area further into the SIGC. A given harmonic order, as it is shown in this paper for the 17th harmonic order (see Fig. 6), can be shifted from the plateau spectral area towards the cutoff. Once the focus is placed further inside the SIGC, fine-tuning via the gas pressure is applicable. As our experiments prove, the spectral distance to the cutoff influences the spatial profile of the harmonic radiation as well, meaning that one can choose the 17th harmonic order to be either in the cutoff with spatial contributions of only one electron trajectory or in the plateau with contributions of long and short electron trajectories together simply by altering the focusing position.

Our findings show that the ability to control the phase-matching conditions in the SIGC is strongly connected to the absorption properties of the generating medium. In order to shift the effective generation volume V_{eff} into the wings of the focus and control phase-matching contributions of the Gouy phase, the harmonic radiation from the center of the focus needs to be reabsorbed; otherwise, the detected signal will be dominated by harmonic radiation from the center of the focus for all focusing positions in the gas cell. This represents a striking difference to phase matching in a gas jet, where the area of the focus which effectively contributes to HHG can be selected by choosing the desired focus position with respect to the medium.

Further investigations need to be done for lower harmonic orders. Based on the phase-matching studies by Steingrube *et al.* [39], we expect the lower harmonic orders to be phase matched in an area around $z_f \geqslant 0$. We anticipate that the features of a decreasing divergence angle are symmetric, leading to a mirrored result as in Fig. 3(b). Additionally, we assume the long trajectory contributions to be favored since the phase-matching conditions are similar to those of a gas jet placed in front of a focus.

VI. CONCLUSION

Our analysis of the spatial beam profile reveals two spatially separated contributions to harmonic radiation, originating from different electron trajectories. The harmonic emission from these trajectories is studied as a function of different phase-matching parameters. Within a thick gas target, we identify a parameter range of the focusing position, where low divergent harmonics are emitted on axis and in a region in which spatial filtering allows separation of the harmonic radiation from different electron trajectory contributions. Detailed measurements of the angular divergence are presented in a SIGC. The divergence angle corresponds to the phase slope α, which exhibits a significant intensity dependence for cutoff harmonics. We observe this behavior through comparison of the ratio of the coherence time $T_{coh}(\text{short})/T_{coh}(\text{long})$ to the ratio of the corresponding divergence angles $\theta_{long}/\theta_{short}$.

The absorption in a SIGC interaction geometry allows for unique phase-matching conditions, influencing the control of electron-trajectory contributions and the harmonic cutoff frequency. Our observations are explained by considering the effective interaction volume for HHG at different pressures and focusing positions inside the gas cell. Simulations confirm the experimental results and prove that the medium absorption is the dominant control parameter for the angular divergence, cutoff tuning, and phase matching.

The presented results show that two strategies can be implemented for attosecond pulse generation, when using a SIGC setup. One way is to generate low-divergence harmonic radiation in a thick target with a focus placed well inside the gas cell. The other way is a focusing position close to the exit pinhole and consecutive spatial filtering of the off-axis electron-trajectory contributions. In both cases one takes advantage of the unique properties of the interaction geometry, allowing for reliable attosecond-pulse light sources with high repetition rates.

ACKNOWLEDGMENTS

The authors thank Vasily V. Strelkov and Pascal Salières for valuable discussions and the Deutsche Forschungsgemeinschaft DFG and the Cluster of Excellence QUEST for financial support of this work. Carlos Hernández-García and Luis Plaja acknowledge support from Junta de Castilla y León (Consejería de Educación and Fondo Social Europeo) and Spanish MINECO (FIS2009-09522).

[1] G. Sansone, L. Poletto, and M. Nisoli, Nat. Photon. **5**, 655 (2011).

[2] M. Hentschel, R. Kienberger, C. Spielmann, G. A. Reider, N. Milosevic, T. Brabec, P. Corkum, U. Heinzmann, and M. Drescher, Nature (London) **414**, 509 (2001).

[3] E. Goulielmakis, M. Schultze, M. Hofstetter, V. S. Yakovlev, J. Gagnon, M. Uiberacker, A. L. Aquila, E. M. Gullikson, D. T. Attwood, R. Kienberger, F. Krausz, and U. Kleineberg, Science **320**, 1614 (2008).

[4] F. Krausz and M. Ivanov, Rev. Mod. Phys. **81**, 163 (2009).

[5] P. B. Corkum, Phys. Rev. Lett. **71**, 1994 (1993).

[6] M. Lewenstein, P. Balcou, M. Y. Ivanov, A. L'Huillier, and P. B. Corkum, Phys. Rev. A **49**, 2117 (1994).

[7] M. Bellini, C. Lyngå, A. Tozzi, M. B. Gaarde, T. W. Hänsch, A. L'Huillier, and C.-G. Wahlström, Phys. Rev. Lett. **81**, 297 (1998).

[8] C. Lyngå, M. B. Gaarde, C. Delfin, M. Bellini, T. W. Hänsch, A. L'Huillier, and C.-G. Wahlström, Phys. Rev. A **60**, 4823 (1999).

[9] P. Salières, T. Ditmire, M. D. Perry, A. L'Huillier, and M. Lewenstein, J. Phys. B: At. Mol. Opt. Phys. **29**, 4771 (1996).

[10] P. Salières, A. L'Huillier, P. Antoine, and M. Lewenstein, Opt. Phys. **41**, 83 (1999).

[11] M. B. Gaarde and K. J. Schafer, Phys. Rev. A **65**, 031406 (2002).

[12] G. Sansone, E. Benedetti, F. Calegari, C. Vozzi, L. Avaldi, R. Flammini, L. Poletto, P. Villoresi, C. Altucci, R. Velotta, S. Stagira, S. D. Silvestri, and M. Nisoli, Science **314**, 443 (2006).

[13] Y. Mairesse, A. de Bohan, L. J. Frasinski, H. Merdji, L. C. Dinu, P. Monchicourt, P. Breger, M. Kovacev, R. T. B. Carre, H. G. Muller, P. Agostini, and P. Salières, Science **302**, 1540 (2003).

[14] R. Lopez-Martens, K. Varjú, P. Johnsson, J. Mauritsson, Y. Mairesse, P. Salières, M. B. Gaarde, K. J. Schafer, A. Persson, S. Svanberg, C.-G. Wahlström, and A. L'Huillier, Phys. Rev. Lett. **94**, 033001 (2005).

[15] C. Hernández-García and L. Plaja, J. Phys. B: At. Mol. Opt. Phys. **45**, 074021 (2012).

[16] P. Salières, P. Antoine, A. de Bohan, and M. Lewenstein, Phys. Rev. Lett. **81**, 5544 (1998).

[17] P. Salières, B. Carrè, L. L. Dèroff, F. Grasbon, G. Paulus, H. Walther, R. Kopold, W. Becker, D. Milosevič, A. Sanpera, and M. Lewenstein, Science **292**, 902 (2001).

[18] M. Lewenstein, P. Salières, and A. L'Huillier, Phys. Rev. A **52**, 4747 (1995).

[19] J.-P. Brichta, M. C. H. Wong, J. B. Bertrand, H.-C. Bandulet, D. M. Rayner, and V. R. Bhardwaj, Phys. Rev. A **79**, 033404 (2009).

[20] J.-F. Hergott, M. Kovacev, H. Merdji, C. Hubert, Y. Mairesse, E. Jean, P. Breger, P. Agostini, B. Carré, and P. Salières, Phys. Rev. A **66**, 021801(R) (2002).

[21] H. Merdji, M. Kovačev, W. Boutu, P. Saliéres, F. Vernay, and B. Carrè, Phys. Rev. A **74**, 043804 (2006).

[22] K. J. Schafer, M. B. Gaarde, A. Heinrich, J. Biegert, and U. Keller, Phys. Rev. Lett. **92**, 023003 (2004).

[23] L. Brugnera, D. J. Hoffmann, T. Siegel, F. Frank, A. Zair, J. W. G. Tisch, and J. P. Marangos, Phys. Rev. Lett. **107**, 153902 (2011).

[24] F. Calegari, C. Vozzi, M. Negro, G. Sansone, F. Frassetto, L. Poletto, P. Villoresi, M. Nisoli, S. D. Silvestri, and S. Stagira, Opt. Lett. **34**, 3125 (2009).

[25] L. E. Chipperfield, J. S. Robinson, J. W. G. Tisch, and J. P. Marangos, Phys. Rev. Lett. **102**, 063003 (2009).

[26] M. Lucchini, F. Calegari, K. Kim, G. Sansone, and M. Nisoli, New J. Phys. **14**, 033009 (2012).

[27] F. Calegari, M. Lucchini, K. S. Kim, F. Ferrari, C. Vozzi, S. Stagira, G. Sansone, and M. Nisoli, Phys. Rev. A **84**, 041802 (2011).

[28] A. Pirri, C. Corsi, E. Sali, A. Tortora, and M. Bellini, Laser Phys. **17**, 138 (2007).

[29] C. Corsi, A. Pirri, E. Sali, A. Tortora, and M. Bellini, Phys. Rev. Lett. **97**, 023901 (2006).

[30] S. Teichmann, D. Austin, P. Bates, S. Cousin, A. Grün, M. Clerici, A. Lotti, D. Faccio, P. Di Trapani, A. Couairon, and J. Biegert, Laser Phys. Lett. **9**, 207 (2012).

[31] F. Schapper, M. Holler, T. Auguste, A. Zair, M. Weger, P. Saliéres, L. Gallmann, and U. Keller, Opt. Express **18**, 2987 (2010).

[32] A. Zaïr, M. Holler, A. Guandalini, F. Schapper, J. Biegert, L. Gallmann, U. Keller, A. S. Wyatt, A. Monmayrant, I. A. Walmsley, E. Cormier, T. Auguste, J. P. Caumes, and P. Salières, Phys. Rev. Lett. **100**, 143902 (2008).

[33] E. Brunetti, R. Issac, and D. A. Jaroszynski, Phys. Rev. A **77**, 023422 (2008).

[34] H. Xu, H. Xiong, Z. Zeng, Y. Fu, J. Yao, R. Li, Y. Cheng, and Z. Xu, Phys. Rev. A **78**, 033841 (2008).

[35] W. Cao, G. Laurent, C. Jin, H. Li, Z. Whang, C. D. Lin, I. Ben-Itzhak, and C. L. Cocke, J. Phys. B: At. Mol. Opt. Phys. **45**, 074013 (2012).

[36] N. Papadogiannis, C. Kalpouzos, E. Goulielmakis, G. Nersisyan, D. Charalambidis, F. Augé, F. Weihe, and P. Balcou, Appl. Phys. B **73**, 687 (2001).

[37] J. Sutherland, E. Christensen, N. Powers, S. Rhynard, J. Painter, and J. Peatross, Opt. Exp. **12**, 4430 (2004).

[38] J. Peatross, J. R. Miller, K. R. Smith, S. E. Rhynard, and B. W. Pratt, J. Mod. Opt. **51**, 2675 (2004).

[39] D. S. Steingrube, T. Vockerodt, E. Schulz, U. Morgner, and M. Kovačev, Phys. Rev. A **80**, 043819 (2009).

[40] M. B. Gaarde, F. Salin, E. Constant, P. Balcou, K. J. Schafer, K. C. Kulander, and A. L'Huillier, Phys. Rev. A **59**, 1367 (1999).

[41] C. Hernández-García, J. A. Pérez-Hernández, J. Ramos, E. C. Jarque, L. Roso, and L. Plaja, Phys. Rev. A **82**, 033432 (2010).

[42] J. A. Pérez-Hernández, L. Roso, and L. Plaja, Opt. Exp. **17**, 9891 (2009).

[43] W. Becker, A. Lohr, M. Kleber, and M. Lewenstein, Phys. Rev. A **56**, 645 (1997).

[44] E. Clementi and C. Roetti, At. Dnto Nucl. Data **14**, 177 (1974).

[45] X. Tong and C. Lin, J. Phys. B **38**, 2593 (2005).

[46] C. Hernández-García, I. Sola, and L. Plaja (unpublished).

[47] V. Platonenko, V. Strelkov, and G. Ferrante, J. Opt. Soc. Am. B **19**, 1611 (2002).

[48] S. Batebi and V. Platonenko, Quantum Electron. **34**, 71 (2004).

[49] P. Balcou, P. Salières, A. L'Huillier, and M. Lewenstein, Phys. Rev. A **55**, 3204 (1997).